Design of A Unified Active Locomotion Mechanism for A Capsule-shaped Laparoscopic Camera System

Xiaolong Liu[1] and Gregory J. Mancini[2] and Jindong Tan[1]

Abstract— This paper proposes a unified active locomotion mechanism for a capsule-shaped laparoscopic surgical camera system. The proposed design integrates the camera's fixation and manipulation together by adjusting a 3D rotational magnetic field from a stator outside a patient's body. The stator generates both torque to rotate the inside rotor dome in all three dimensions, and force to serve as an anchoring system that keeps the camera steady during a surgical procedure. This design eliminates the need for an articulated design and therefore the integrated motors to significantly reduce the size of the camera. A set of stator and rotor designs are developed and evaluated by simulations and experiments.

I. INTRODUCTION

SINGLE-PORT surgery is a popular minimally invasive surgery technique. A single small incision or a natural orifice in human anatomy is adopted for inserting surgical instruments and laparoscopic cameras through the incision. Laparoscopic cameras play a key role that feedbacks visual information to guide surgical procedures. A standard trocar laparoscopic camera is mostly adopted by pushing a long stick through an incision. However, a shared incision limits the dexterity of surgical instruments and the field of views of laparoscopic cameras.

Considering the limitations of a conventional laproscopic camera, it is more desirable to have a surgical camera system which can be actively controlled for adjusting the camera's visualization target. One of the research challenges for such a camera system is the development of its locomotion mechanism. There are two main problems for designing the locomotion mechanism: fixation that holds the camera in a stable position and manipulation that actuates the camera to its desired visualization target direction.

The state-of-the-art techniques for fixating the inserted cameras are categorized as suturing the cameras against abdominal wall or piercing the cameras into the abdominal wall by needles; and applying external permanent magnets (EPMs) to attract the camera magnetically. The manipulation techniques of the cameras consist of motor-driven, magnet assisted motor-driven, and magnetic driven techniques. Hu *et al.* developed two tethered laparoscopic cameras which adopt DC servo motors assisted with a worm gear mechanism to enable a pan motion and tilt motion separately [1], [2]. For the camera's fixation of both of their designs, they are sutured against the abdominal wall. Castro *et al.* proposed
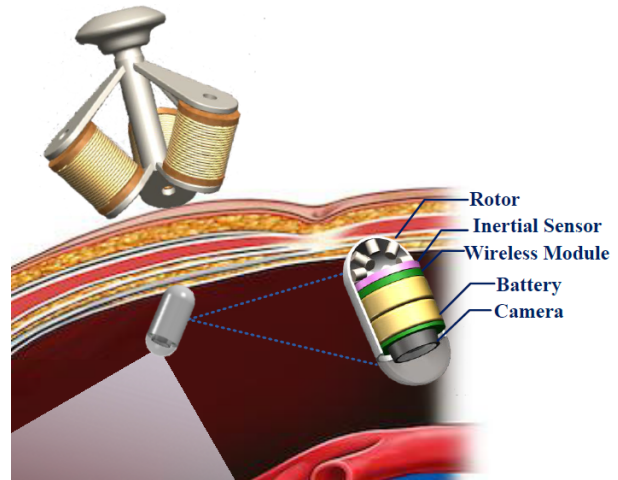

Fig. 1. Concept of the capsule-shaped laparoscopic camera system.

a wireless miniature anchored laparoscopic camera which applies a needle to pierce through a patient's abdominal wall for the camera fixation, and is manipulated by two motors for pan and tilt motions. However, the major drawback of a suturing or piercing fixation is not only does this method injure the patient's body but it also leads to poor flexibility for translating the device to a new desired location.

Different from the suturing or piercing fixation, EPMs provide an alternative way by magnetic forces. Platt *et al.* proposed a ceiling pan/tilt camera design which has a cylindrical housing with attached magnetic caps at both ends [3]. An EPM handle allows surgeons to pan the camera outside patient's abdominal wall while a motor inside the camera drives itself for a tilt motion. Valdastri *et al.* designed a wireless laparoscopic camera system which embeds two donut-shaped magnets and a motor in a capsule-shaped housing, and applies an EPM for anchoring the location and generating a tilt motion of the camera [4]. Two modified designs of [4] are proposed in [5], [6].

Research efforts so far have addressed separate mechanisms for locomotion in the body cavity and pan/tilt of the camera, which results in bulky articulated systems and only limited degrees of freedom for locomotion and camera control. Therefore, a unified active locomotion mechanism is desired by integrating the fixation and manipulation mechanisms together. Compared with laparoscopic camera systems, some state-of-the-art endoscopic systems have applied magnetic guidance for locomotion of capsule endoscopes. Sendoh *et al.* proposed a capsule-shaped endoscopic camera

---

[1]Xiaolong Liu and Jindong Tan are with Department of Mechanical, Aerospace and Biomedical Engineering, University of Tennessee, Knoxville, TN 37996, USA xliu57@utk.edu,tan@utk.edu

[2]Gregory J. Mancini is with Department of Surgery, University of Tennessee, Knoxville, TN 37996, USA GMancini@mc.utmck.edu

with a permanent magnet inside the capsule and a spiral structure outside the capsule, is actuated by an external rotational magnetic field [7]. Ciuti *et al.* proposed a gastrointestinal tract inspection endoscopic camera which adopts an EPM installed robot end-effector to actuate the camera with four identical axially magnetized cylinder magnets inside [8]. However, the locomotion mechanisms of the endoscopic cameras are not suitable to be used in a laparoscopic camera because the structures of an abdominal cavity and GI tract are quite different.

Inspired by spherical actuators [9], [10], [11], we propose a novel motor-free unified active locomotion mechanism for a laparoscopic camera, as shown in Fig. 1. Similar to a rotor in a spherical actuator, a set of magnets arranged at the semi-spherical dome can be magnetically coupled to a stator placed outside patient's body against or close to the dermal surface. The coils generate a 3D rotational magnetic field, thereby generating both torque to rotate the inside rotor dome in all three dimensions, and force to serve as an anchoring system that keeps the camera steady during a surgical procedure. This design eliminates the need for an articulated design and therefore the integrated motors to significantly reduce the size of the camera. This design enables the unified translational and rotation controls with the external device.

However, different from a spherical actuator, the distance from the camera's rotor to a stator is much longer in the surgical situation due to the thickness of patient's abdominal wall. The magnetic force and torque will rapidly reduce while the distance from a rotor to a stator increases. Only improving the input currents cannot solve this problem because of the limited power supply and coils's overheating. In order to address the problems mentioned above, a set of rotor and stator designs are proposed and evaluated in this paper for achieving a reliable laparoscopic camera system.

II. CONCEPT AND ROTOR/STATOR DESIGNS OF WIRELESS LAPAROSCOPIC CAMERA SYSTEM

The objective of this paper emphasizes on developing a reliable camera's locomotion mechanism. The remaining components will be discussed in the future works. In this section, the configuration of the camera system will be introduced. And three stator and four rotor designs are proposed.

A. Configurations of the Camera System

The laparoscopic camera system consists of two parts: a rotor embedded capsule-shaped camera and a coil winding stator. The camera consists of five main components, as shown in Fig. 1: a semi-spherical magnetic head for locomotion, an illumination and a camera module for visualization, a battery and a battery management module for power supply, a wireless communication module for data transmission, and an inertial sensing module for controlling. Our proposed camera has two semi-spherical domes, one for housing the illumination and the camera module; the other for housing the small cylindrical magnets which serve as the driving unit
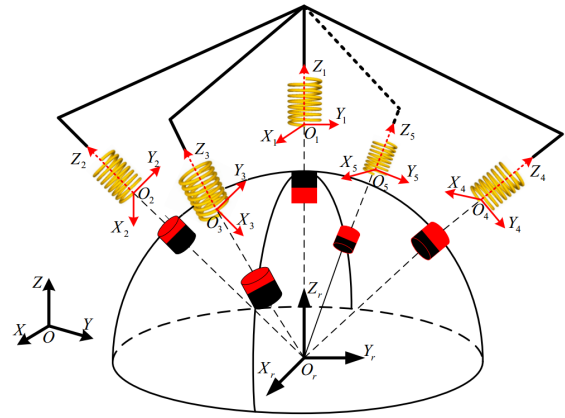

Fig. 2. The working principle of the spherical motor inspired locomotion mechanism.

in the camera system. The stator consists of multiple coils which are distributed around a virtual dome to simulate part of a stator of a spherical motor. The adjustable currents in the coils provide attracting force and rotating torque to fixate and manipulate the camera.

The working principle of the proposed design can be illustrated in Fig. 2. The system is designed to enable two types of motions for the camera system, navigation (translational control) and orientation control, in addition to the compensation of the gravity of the camera. The singularityless orientation control requires torque along three axes of camera system, and the translation control requires forces along three axes, with the force along z axis providing the fixation of the camera against the abdominal wall. By varying the input currents of all coils which coordinate at $\Sigma_j = \{X_j, Y_j, Z_j\}$, any desirable rotation can be achieved for the rotation control of the camera by the generated rotational magnetic field. The navigational control of the camera is provided by moving the passive fixture along the dermal surface with the attractive forces between the permanent magnets and coils. To simplify the analysis of our proposed designs, Σ_r and Σ_j are all referred to a common reference frame $\Sigma = \{X, Y, Z\}$ by assuming Σ 's origin O locates at O_r.

B. Stator Designs

The number of the coils in a stator should be at least four because of the camera's three degrees of freedom orientation mobility (1 for camera fixation in Z direction, 3 for camera orientation). But in fact, the rotation around capsule's long axis is not as important as the other two rotations due to the camera's symmetry structure along its long axis. Therefore, the coil's number of a stator can be extended to 3.

Considering a proper size of the stator, the designs consist of 3, 4, and 5 coils respectively as shown in Fig. 3 (a), (c), (d). To simplify the stator designs, all the coils share the same dimension: an outer radius R, an inner radius r, a coil height h and a tilt angle ψ. Taking the 3 coil stator as an example, the initial setting assumes all the coils are tangent to each other in the XY plane with $\psi = 0$, as shown in Fig. 3(a).
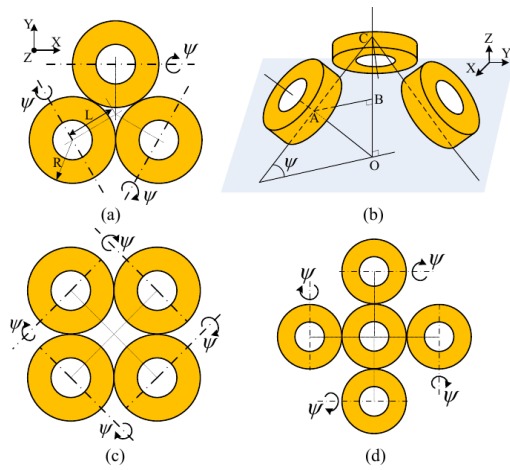
Fig. 3. Three stator designs.

(a) Rotor model 1

(b) Rotor model 2

(c) Rotor model 3

(d) Rotor model 4

Fig. 4. Four rotor designs.

The ψ rotating axises are fixed at the bottoms of the coils. To calculate ψ, the coil to rotor distance d has to be determined. According to the reference [12], the average thickness of the abdominal wall is about $30\,\mathrm{mm}$. For compensating a titled depth of the stator, d is set as $40\,\mathrm{mm}$. As illustrated in Fig. 3 (b) where $OA = d$, $AB = L$, ψ can be calculated by $\arcsin(L/d)$. Considering the weak magnetic flux density generated by air-core coils, soft iron rods are inserted coils in the coils for producing stronger magnetic field. Similar calculations are applied to 4 and 5 coils stators in Fig. 3(c) and (d). In the 5 coil stator design, there is no tilt angle on the central coil.

C. Rotor Designs

For designing the rotor, a set of axially magnetized cylinder magnets are embedded in the semi-spherical dome of the camera. In this paper, four rotor designs are proposed as shown in Fig. 4. The red magnets represent the north poles pointing outside or upside while the blue ones point to the opposite ways. Rotor design 1 and 4 in Fig. 4(a), (d) both include a disc magnet. It is worth noting that a disc magnet and a cylinder magnet can both be considered as a magnetic dipole in the far field. This fact will be used for developing the analytical model of the locomotion mechanism in Section III. The rotor 1 in Fig. 4(a) consists of 12 small cylinder magnets that are mounted along the equator at the longitude of every $60°$, along the latitude of $60°$ at the longitude of every $60°$. Rotor 2 in Fig. 4(b) consists of 13 small cylinder magnets which are mounted along the equator at the longitude of every $45°$, along the latitude of $45°$ at the longitude of every $90°$, and one on the north pole. Rotor 3 shown in Fig. 4(c) is similar to model 2 with the only difference that the magnets are mounted along the latitude of $45°$ at the longitude of every $45°$. Rotor 4 adds a disc magnet based on model 3.

D. Design Parameters

The purpose of proposing different designs aims at seeking reasonable models and parameters for a reliable camera
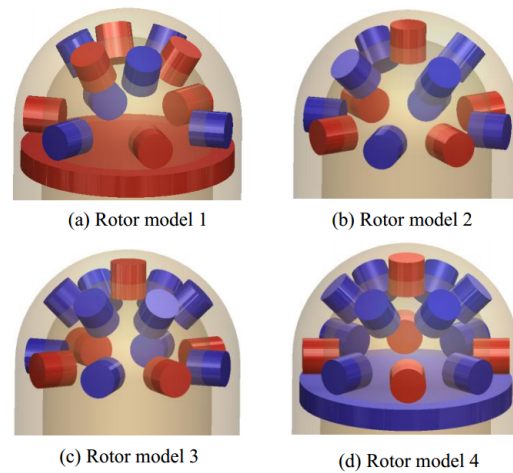
locomotion mechanism. Therefore, a set of parameters of the stator and rotor has to be specified. The outer radius R of the coils ranges from $8\,\mathrm{mm}$ to $30\,\mathrm{mm}$, the inner radius and coil height are fixed at $5\,\mathrm{mm}$ and $30\,\mathrm{mm}$ respectively. The reason for fixing the inner radius and coil height is because changing the two parameters will not significantly affect the generated force and torque compared with the outer radius R according to our preliminary experiments. Considering the dimension of the camera whose dome has a $8\,\mathrm{mm}$ inner radius and commercially available cylinder magnets, the radius and height of a cylinder magnet are selected as $1.27\,\mathrm{mm}$ and $2.54\,\mathrm{mm}$ separately with residual magnetization as $1.32\,\mathrm{Tesla}$. The disc magnet is chosen as $1.59\,\mathrm{mm}$ height and $8\,\mathrm{mm}$ radius with its residual magnetization as $1.43\,\mathrm{Tesla}$.

The current density in the coils has a major impact on the generated force and torque. The maximum current carrying capacity of a coil is determined by a copper wire's cross sectional area. In this paper, we select copper wire's with a cross sectional area as $1\,\mathrm{mm}^2$. In terms of experiential data, a $1\,\mathrm{mm}^2$ copper wire can carry less than $8\,\mathrm{A}$ for long-time duty and less than $16\,\mathrm{A}$ for short-time duty. The current carrying capacity also depends on insulation materials and cooling conditions. For testing our designs, we safely assume the maximum current carrying capacity $|I_{max}|$ is $5\,\mathrm{A}$.

III. MODELING OF THE UNIFIED LOCOMOTION MECHANISM

The objective of building the analytical model of the camera system's locomotion mechanism is twofold: to realize real-time dynamic control of the laparoscopic camera by changing the input currents; and to analyze the control capabilities of various rotor and stator designs. In this paper, we focus on evaluating the control capabilities of our proposed designs based on the analytical model. The central problem of developing the analytical model is how to calculate the force and torque generated on the rotor. The techniques applied to spherical motors for deriving their dynamic analytical model are all based on Lorentz law due to

the air-core coils [9], [10], [11]. However, in our application the thickness of the abdominal wall is much greater than the air gap in the spherical motors. Compared with air core coils, iron-core coils can provide stronger magnetic field because of the high magnetic permeability of soft iron. Thus in this paper, both air-core and iron-core coils will be considered. The Lorentz force law can not handle the analytical model with iron-core coils. Considering the shapes of the cylinder/disc magnets in the semi-spherical dome of the camera, the magnetic moment of each magnet can be described as $\mathbf{M}$. The force and torque applied on a magnet with its magnetic moment $\mathbf{M}$ can be represented by

$$\mathbf{T} = \mathbf{M} \times \mathbf{B}, \tag{1}$$
$$\mathbf{F} = (\mathbf{M} \cdot \nabla)\mathbf{B}, \tag{2}$$

where $\mathbf{B}$ is the magnetic flux density at the location of $\mathbf{M}$ [13]. To analyze the generated force and torque, the rotor's magnetic moment $\mathbf{M}$ and the stator's magnetic flux density $\mathbf{B}$ have to be calculated.

A. Stator's Magnetic Flux Density $\mathbf{B}$

For modeling the stator's magnetic flux density, a set of local coordinate systems of the coils are set as $\Sigma_1 = \{X_1, Y_1, Z_1\}$, $\Sigma_2 = \{X_2, Y_2, Z_2\}$, ..., $\Sigma_N = \{X_N, Y_N, Z_N\}$ where N is the number of the coils. The representations of $\mathbf{M}$ and $\mathbf{B}$ in (1) and (2) have to share the same coordinate system. Therefore, a reference frame $\Sigma = \{X, Y, Z\}$ is adopted for establishing the relationship between the stator's coordinates and rotor's coordinates. The transformation from local coil coordinates $\Sigma_j = \{X_j, Y_j, Z_j\}$ to a reference coordinates $\Sigma = \{X, Y, Z\}$ can be expressed as

$$\mathbf{P}_j = \mathbf{R}_j \mathbf{P} + \mathbf{T}_j, \tag{3}$$

where $\mathbf{P} = (x, y, z)$ and $\mathbf{P}_j = (x_j, y_j, z_j)$ are the same point in different coordinates Σ and Σ_j, and $j = 1, ..., N$. $\mathbf{R}_j$ and $\mathbf{T}_j$ are the rotational matrix and translational vector from Σ_j to Σ respectively.

The magnetic flux density at a point in space can be superimposed from each coil in a reference coordinates Σ

$$\mathbf{B}(x, y, z) = \sum_{j=1}^{N} \mathbf{R}_j^T \mathbf{B}_j(x_j, y_j, z_j), \tag{4}$$

where $\mathbf{B}_j$ is the coil's magnetic flux density in its local coordinates. Considering we have an air-core and an iron-core options for the coils, it is preferred to have a common representation of the coil's magnetic flux density. Finite Element Method (FEM) is able to obtain accurate solutions of the coil's magnetic flux density by building extra fine meshes. However, the expensive computational time of FEM fails itself to serve in a real time application. A magnetic dipole model fitting method proposed in [14], which adopts the coil's axial magnetic flux density simulation results from Finite Element Method as the fitting data, is applied for estimating the parameter p and l in

$$\mathbf{B}_j(\mathbf{P}_j) = \frac{\mu_0}{4\pi} \left(-\frac{\mathbf{M}}{|\mathbf{P}_j|^3} + \frac{3(\mathbf{M} \cdot \mathbf{P}_j)\mathbf{P}_j}{|\mathbf{P}_j|^5} \right), \tag{5}$$

where $\mathbf{M} = p\mathbf{l}$ is the coil's equivalent magnetic moment. It has been verified in [14] the magnetic flux density $\mathbf{B}_j$ has a linear relationship with input current I_j. Thus, (4) can be reformulated as

$$\mathbf{B}(x, y, z) = \sum_{j=1}^{N} \mathbf{R}_j^T \mathbf{B}_j^u(x_j, y_j, z_j) I_j, \tag{6}$$

$\mathbf{B}_j^u$ is the unit magnetic flux density of coil j.

B. Rotor's Magnetic Moment $\mathbf{M}$

The complex structures of the rotor designs make it difficult to express the rotor's magnetic moment in one piece. Because the forces and torques applied on each individual magnet can be superimposed in a linear way, a strategy for expressing the rotor's magnetic moment is to establish the relationship between each magnet's magnetic moment and the magnetic flux density generated from each coil.

In the rotor's local coordinates $\Sigma_r = \{X_r, Y_r, Z_r\}$, the cylindrical magnets are distributed around the semi-spherical dome, as shown in Fig. 2. The orientation and position of the magnets in Σ_r are arranged as $\mathbf{R}_i^m$ and $\mathbf{T}_i^m$, $i = 1, ..., n$, n is the number of the cylindrical magnets. The magnetic moment of the ith magnet in Σ_r is expressed as

$$\mathbf{M}_i^r = m_i \cdot \mathbf{d}_i, \tag{7}$$

where the value of the magnetic moment m_i can be calculated from

$$m_i = \frac{1}{4} M_0 \pi D_i^2 L_i, \tag{8}$$

M_0 is the residual magnetization of the cylinder magnet, D_i and L_i are the diameter and height of the ith cylinder [15]. $\mathbf{d}_i$ is the magnet's orientation which is calculated by $\mathbf{d}_i = \mathbf{R}_i^m (0, 0, 1)^T$. Due to the rotor's rotational motion characterized by a rotational matrix $\mathbf{R}$ in the reference coordinates Σ, the transformation from Σ_r to Σ is represented by

$$\mathbf{P}_r = \mathbf{R}\mathbf{P} + \mathbf{T}, \tag{9}$$

where $\mathbf{P}_r$ denotes a point in Σ_r. $\mathbf{R}$ and $\mathbf{T}$ are the rotational and translational vectors from Σ_r to Σ. With (9) and (3), the transformation is established between the rotor and stator by

$$\mathbf{P}_j = (\mathbf{R}_j \mathbf{R}^T)(\mathbf{P}_r - \mathbf{T}) + \mathbf{T}_j, \tag{10}$$

which will be used to represent $\mathbf{M}$ and $\mathbf{B}$ in a common coordinates in order to calculate the force and torque in (1) and (2).

C. Force and Torque Calculation

Because magnetic forces contribute part of magnetic torques, shifting the magnet's rotational centers to the semi-spherical rotor's center is necessary for superimposing the force-contributed torques generated on different magnets. According to what we have discussed in Section III-A, III-B

and (1)-(2), the unit force and torque generated on the rotor from a single coil j are formulated as

$$\mathbf{F}_j^u = \sum_{i=1}^n (\mathbf{M}_i^j \cdot \nabla)\mathbf{B}_j^u, \qquad (11)$$

$$\mathbf{T}_j^u = \sum_{i=1}^n [\mathbf{M}_i^j \times \mathbf{B}_j^u + \mathbf{L}_i \times (\mathbf{M}_i^j \cdot \nabla)\mathbf{B}_j^u]. \qquad (12)$$

where $\mathbf{L}_i$ is the ith magnet's lever arm; $\mathbf{M}_i^j$ is the ith magnetic moment represented in coil coordinates Σ_j and calculated by

$$\mathbf{M}_i^j = (\mathbf{R}_j \mathbf{R}^T) \cdot \mathbf{M}_i^r. \qquad (13)$$

For deriving the complete force and torque equations, $\mathbf{F}_j^u$ and $\mathbf{T}_j^u$ have to be transformed in the common reference coordinates Σ by the rotational matrix $\mathbf{R}_j^T$. Denoting the input current as $\mathbf{I} = (I_1, I_2, ..., I_N)^T$, the final expression of electromagnetic force and torque in reference coordinates Σ can thus be formulated as

$$\mathbf{F} = \sum_{j=1}^N \mathbf{R}_j^T \mathbf{F}_j^u I_j, \qquad (14)$$

$$\mathbf{T} = \sum_{j=1}^N \mathbf{R}_j^T \mathbf{T}_j^u I_j. \qquad (15)$$

Considering the force analysis of the laparoscopic camera inside a patient's abdominal cavity, the forces applied on the camera can be categorized as the electromagnetic force $\mathbf{F}$, the membrane force $\mathbf{f}_m$ from the squeezed abdominal cavity wall tissue, the liquid friction force $\mathbf{f}_l$ while the camera is transitioning and rotating, and the camera's gravity force $m\mathbf{g}$. The electromagnetic force $\mathbf{F}$ will balance all the other forces. Assume $\mathbf{p}$ is the camera's location in the reference coordinates Σ. In accordance to Newton's law, the dynamic model of the camera can thus be expressed as

$$m\ddot{\mathbf{p}} = \mathbf{F} - \mathbf{f}_l - \mathbf{f}_m - m\mathbf{g}. \qquad (16)$$

It is important to note in (16) that the Z component of the electromagnetic force f_z will lead to the tissue deformation and subsequently changes $\mathbf{f}_l$ and $\mathbf{f}_m$. To maximally eliminate the torques generated from $\mathbf{f}_l$ and $\mathbf{f}_m$ when the camera is steering, one control strategy to deal with this problem is that before manipulating the camera, reduce f_z for alleviating the effects of $\mathbf{f}_l$ and $\mathbf{f}_m$ on the camera. After actuating, increase f_z for applying the torques generated from $\mathbf{f}_l$ and $\mathbf{f}_m$ to balance the torque from the camera's gravity force.

IV. SIMULATION AND EXPERIMENTAL RESULTS

In this section, the prototype designs of our proposed laparoscopic camera system are fabricated and evaluated based on the developed analytical model of the locomotion mechanism. To analyze the analytical model of stator's magnetic flux density, the data from a FEM software is adopted as a benchmark. The maximum output forces and torques of different designs are compared in accordance with analytical solutions. At last, the generated forces and torques of the fabricated stator and rotor are tested by real force/torque sensors.
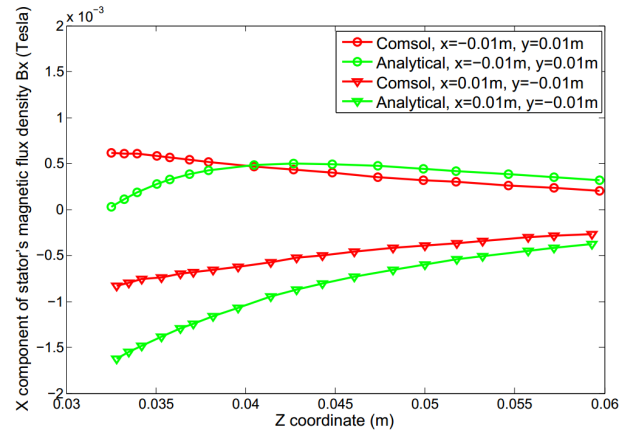
(a) B_x component magnetic flux density
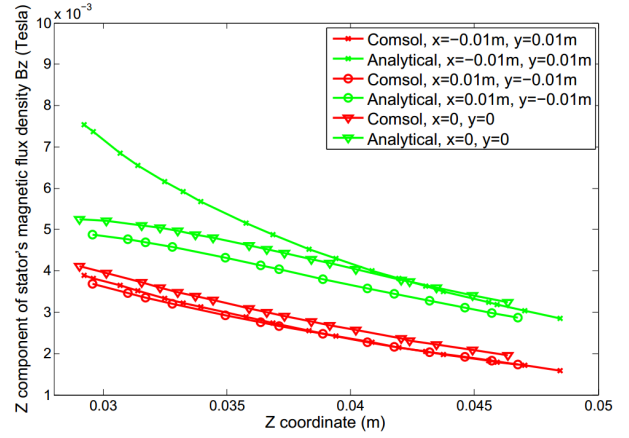
(b) B_z component magnetic flux density

Fig. 5. Stator's magnetic flux density evaluation.

A. Simulation Results

1) Stator's Magnetic Flux Density Evaluation: For evaluating the analytical model of the iron-core stator's magnetic flux density developed in Section III-A, a set of FEM simulation data obtained from COMSOL Multiphysics 4.3a (COMSOL Inc., Sweden) are used to compare with our analytical results. As shown in Fig. 5, the analytical magnetic flux density of the stator is estimated by FEM. The parameters m and l for the magnetic dipole model in (5) are calculated as $m = 2.98\,\text{Am}^2$ and $l = 0.44\,\text{m}$. The origin of the stator coordinates $\Sigma_s = \{X_s, Y_s, Z_s\}$ is located at the geometric center of the three origins of coil coordinates. The direction Z_s is determined by summing the vectors $\mathbf{Z}_1$, $\mathbf{Z}_2$, and $\mathbf{Z}_3$ in Σ. Fig. 5(a) and 5(b) show the comparison results of B_x and B_z in the working region which is along negative Z_s direction ranging from $0.03\,\text{m}$ to $0.05\,\text{m}$ with two sets of x-y coordinates $\{x_s = 0.01\,\text{m}, y_s = -0.01\,\text{m}\}$ and $\{x_s = -0.01\,\text{m}, y_s = 0.01\,\text{m}\}$. Due to the stator's symmetric structure, B_y can be referred to B_x. As illustrated in Fig. 5, B_z has a major contribution to the generated force and torque because of being much greater than B_x.

2) Stator's Design Evaluation: Table I, II and III show the three stator models' evaluation results based on a common rotor 1. The maximum force and torque components in x,
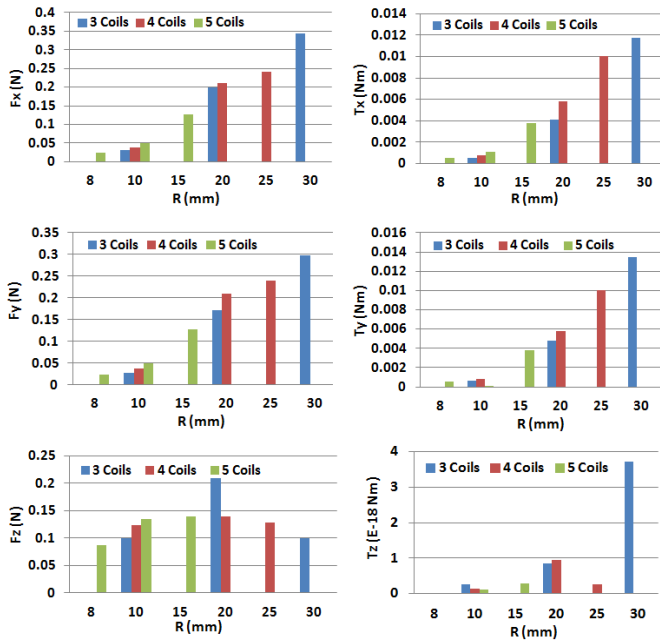
Fig. 6. Stator design comparisons.

Fig. 7. The fabricated rotors and stator.

y, z directions are evaluated under the input current range $-5\,\text{A} \sim 5\,\text{A}$. With a fixed rotor to coil distance as $d = 40\,\text{mm}$, we testify the coil radius $10\,\text{mm}$, $20\,\text{mm}$, $30\,\text{mm}$ on the 3 coil stator, $10\,\text{mm}$, $20\,\text{mm}$, $25\,\text{mm}$ on the 4 coil stator, and $8\,\text{mm}$, $10\,\text{mm}$, $15\,\text{mm}$ on the 5 coil stator. The reason for not applying the same set of radius on all the stator models is because a large radius R for 4 and 5 coil stator will lead ψ to approach to $90°$. It is shown in Table I, II and III that an iron-core stator can generate much greater force and torque than an air-core stator under the same set of design parameters. To clarify the evaluation results, the iron-core experimental results are visualized as shown in Fig. 6. The maximum force and torque in x and y directions are rapidly increasing when outer radius R and tilt angle ψ are growing. But the force component in z direction drops down after the tilt angle ψ pasts over $45°$. The 5 coil stator is a special case which shows that $\psi = 48.6°$ still keeps a growing trend of F_{zmax} value due to the effect of central coil. The torque values T_z along the camera's axis have a e^{-18} number scale which means the camera cannot be rotated around its Z_r axis. This fact is actually reasonable because in a real application the camera will not be required to rotate around its own Z_r axis.

Comparing the three models in Table I, II and III, the 3 coils iron-core stator with $R = 20\,\text{mm}$ and the 4 coils iron-core stator with $R = 20\,\text{mm}, 25\,\text{mm}$ provide reasonable forces and torques in all x, y, and z directions. In a real surgery situation, a small tilt angle ψ design is preferred because a larger ψ leads to a greater distance from the rotor to the stator. Therefore, the 3 coil stator with $R = 20\,\text{mm}$ is selected as a candidate design and used in the rotor models evaluation due to its good balance of coil tilt angle ψ and generated forces and torques.
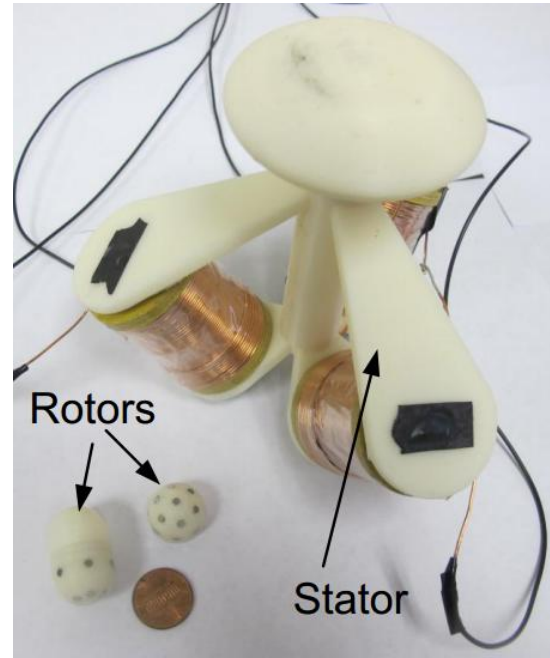
3) Rotor's Design Evaluation: Table IV shows the evaluation results of four rotor designs based on the 3 coil iron-core stator with $R = 20\,\text{mm}$. Rotor 1 and 4 generate greater forces and torques than those generated in the rotor 2 and 3 due to the disc magnet. Rotor 3 has a better performance than rotor model 2. To analyze if the design of our active locomotion system works well, the camera dynamics and abdominal wall tissue model have to be involved. Being evaluated by the Solidworks software, the camera weights approximately 15 grams, and the distance from the gravity center to rotor's center is about $10\,\text{mm}$. The threshold force and torque to actuate the camera are $0.147\,\text{N}$ and $0.001\,47\,\text{Nm}$ which indicates the rotor 1 and 4 are capable of providing enough force and torque for the locomotion mechanism.

B. Camera System Fabrication

1) Rotor Fabrication: Since the objective of this paper is to develop the locomotion mechanism, only the rotor is designed and fabricated in the capsule-shaped camera with leaving out the other components. According to the analytical evaluations of the rotors in Table IV, rotor 4 is selected due to yielding the best force and torque performance among all four rotor designs. The sizes of the small cylinder magnets and the disc magnet are $1/10'' \times 1/10''$ (K&J Magnetics, NdFeB N42) and $5/8'' \times 1/16''$ (K&J Magnetics, NdFeB N52) with their residual magnetizations as $1.32\,\text{Tesla}$ and $1.43\,\text{Tesla}$ respectively. Based on the size of these commercially available magnets, the size of the capsule-shaped camera is designed as $0.75'' \times 1.18''$. A 3D printer is used for building the real rotor models which are shown in Fig. 7.

2) Stator Fabrication: According to the analytical evaluation in Table I, II, III, the 3 coils iron-core stator with $20\,\text{mm}$ outer radius shows the best balance of reasonable dimension

TABLE I
3 COIL STATOR MODELS EVALUATION BASED ON ROTOR 1 CONFIGURATION

Core Type	R (mm)	ψ (°)	F_{xmax} (N)	F_{ymax} (N)	F_{zmax} (N)	T_{xmax} (Nm)	T_{ymax} (Nm)	T_{zmax} (Nm)
	10	16.8	0.0023	0.0020	0.0073	4.08e-5	4.71e-5	2.03e-20
Air Core	20	35.3	0.0374	0.0324	0.0395	7.79e-4	8.99e-4	1.38e-19
	30	60	0.0991	0.0858	0.0286	3.40e-3	3.90e-3	2.72e-15
	10	16.8	0.0318	0.0275	0.1004	5.65e-4	6.52e-4	2.68e-19
Iron Core	20	35.3	0.1983	0.1718	0.2099	4.10e-3	4.80e-3	8.40e-19
	30	60	0.3441	0.2980	0.0993	1.17e-2	1.35e-2	3.71e-18

TABLE II
4 COIL STATOR MODELS EVALUATION BASED ON ROTOR 1 CONFIGURATION

Core Type	R (mm)	ψ (°)	F_{xmax} (N)	F_{ymax} (N)	F_{zmax} (N)	T_{xmax} (Nm)	T_{ymax} (Nm)	T_{zmax} (Nm)
	10	20.7	0.0027	0.0027	0.0090	5.76e-5	5.76e-5	9.13e-20
Air Core	20	45	0.0396	0.0396	0.0264	1.10e-4	1.10e-4	2.86e-20
	25	61.9	0.0438	0.0438	0.0235	1.80e-3	1.80e-3	9,85e-20
	10	20.7	0.038	0.038	0.1244	7.97e-4	7.97e-4	1.36e-19
Iron Core	20	45	0.2103	0.2103	0.1402	5.80e-3	5.80e-3	9.40e-19
	25	61.9	0.2405	0.2405	0.1291	1.00e-2	1.00e-2	2.62e-19

TABLE III
5 COIL STATOR MODELS EVALUATION BASED ON ROTOR 1 CONFIGURATION

Core Type	R (mm)	ψ (°)	F_{xmax} (N)	F_{ymax} (N)	F_{zmax} (N)	T_{xmax} (Nm)	T_{ymax} (Nm)	T_{zmax} (Nm)
	8	23.6	0.0013	0.0013	0.0048	2.80e-5	2.80e-5	1.19e-21
Air Core	10	30	0.0036	0.0036	0.0097	8.15e-5	8.15e-5	4.49e-21
	15	48.6	0.0164	0.0164	0.0179	4.88e-4	4.88e-4	3.18e-20
	8	23.6	0.0237	0.0237	0.0871	5.09e-4	5.09e-4	2.17e-20
Iron Core	10	30	0.0497	0.0497	0.1340	1.10e-3	1.10e-3	1.05e-19
	15	48.6	0.1274	0.1274	0.1391	3.80e-3	3.80e-3	2.88e-19

TABLE IV
ROTOR MODELS EVALUATION UNDER 3 COILS STATOR WITH R=20 mm, IRON CORE.

Rotor models	F_{xmax} (N)	F_{ymax} (N)	F_{zmax} (N)	T_{xmax} (Nm)	T_{ymax} (Nm)	T_{zmax} (Nm)
Model 1	0.1983	0.1718	0.2099	4.10e-3	4.80e-3	8.40e-19
Model 2	0.0091	0.0079	0.0097	2.89e-4	3.34e-4	2.54e-19
Model 3	0.0153	0.0132	0.0162	4.89e-4	5.65e-4	2.37e-19
Model 4	0.2136	0.1850	0.2261	4.60e-3	5.30e-3	2.42e-18

and sufficient force and torque for manipulating the camera. Therefore, in this paper we fabricate this stator design for experimental test, as shown in Fig. 7. The coils are wound by 600 turns copper ware with $1\,\text{mm}^2$ cross sectional area. The height, outer radius and inner radius of each of the coils are $40\,\text{mm}$, $20\,\text{mm}$, and $5\,\text{mm}$ respectively. The resistance of each coil is about $1.3\,\Omega$. The soft iron rods applied in the coils are $9.5\,\text{mm}$ in diameter and $60\,\text{mm}$ in height with their maximum magnetic permeability $2000\,\text{H/m}$. In order to provide controllable independent current inputs for each of the coils, three DC power supplies (Mastech HY5020E) with a maximum output voltage $50\,\text{V}$ and maximum current output $20\,\text{A}$ are adopted for driving the camera's transitional and rotational motions.

C. Force and Torque Measurement Experiments

For validating the analytical model and the maximum generated forces/torques, experiments are set up based on our fabricated rotor and stator. The magnetic force and torque are measured by Barrett WAM arm's Six-Axis Force/Torque sensor with $50\,\text{mN}$ force sensing resolution and $1.5\,\text{mN-m}$ torque sensing resolution. In both of the force and torque measurements, the z axis of the rotor Z_r is assigned to coincide with the symmetry axis of the stator. And the distance from the coils to the center of the rotor is set as $40\,\text{mm}$. For measuring the magnetic force and torque, the locomotion mechanism is placed upside down, as shown in Fig. 8. An "L" shaped lever arm connects the rotor model 4 on one side, and is attached to the F/T sensor on the other side.

The forces along Z_r axises are measured under various current input limits from 0 to $5\,\text{A}$. And the torques are measured around X_r axis. Due to the torque sensing resolution, the F/T sensor is not capable of recording the generated torque according to the simulation results in Table I–IV. Therefore, the lever arm is used to amplify torque measurements for compensating the limits of the sensor. Figure. 9 compares the measurements and simulation results of the generated force and torque. For measuring F_z, all the coils are applied the same current value and direction ranging from 0 to $5\,\text{A}$. In order to measure F_y and T_x, the current of the coil on Y_rZ_r plane ranges $0 \sim -5\,\text{A}$ with the other coils keeping a constant current input $5\,\text{A}$. The preliminary comparison results indicate that the simulation results from
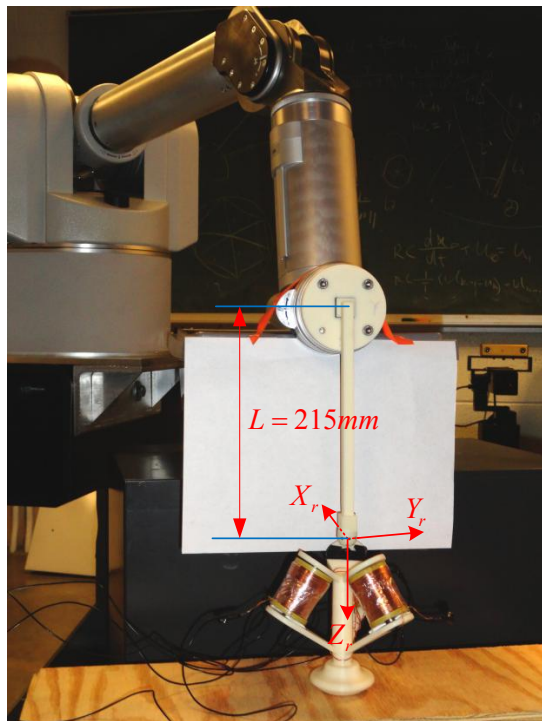
2455

Fig. 8.   The force and torque measurement setups.

Fig. 9.   Force and torque comparison results between measurements and simulations.

our developed analytical model agrees with the measurement results from the F/T sensor.

V. CONCLUSIONS AND FUTURE WORK

In this paper, we propose an innovative active locomotion mechanism for a wireless laparoscopic camera. The locomotion mechanism naturally enables a unified control of transition and orientation for the camera by varying the input current of stator's coils. This design eliminates the need for an articulated design and therefore the integrated motors to significantly reduce the size of the camera. Three stator designs and four rotor designs are developed and evaluated by simulations and experiments for testing manipulation capability of different designs. According to the simulation and experimental results, our proposed designs are able to provide sufficient force and torque to translate and rotate a laparoscopic camera inside patient's abdominal cavities.

Based on the proposed locomotion mechanism designs of camera system, the other components such as a camera module, batteries, a wireless module, inertial sensors will be designed and fabricated in the laparoscopic camera. For manipulating the camera in a surgical situation, a closed loop controller will be developed for the camera system to enable robust and accurate transitional/orientation controls. Various thickness of abdominal walls will be adopted to evaluate the laparoscopic camera system.

REFERENCES

[1] T. Hu, K. Allen, and L. Fowler, "In-vivo pan/tilt endoscope with integrated light source," in *2007 IEEE/RSJ International Conference on Intelligent Robots and Systems*, pp. 1284 –1289, 2007.
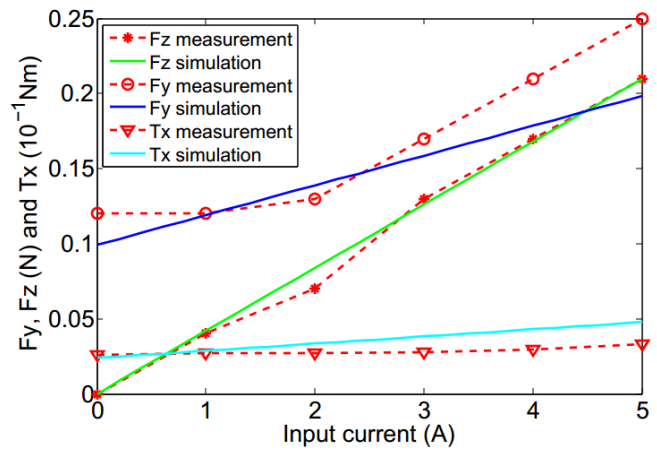
[2] T. Hu, K. Allen, J. Hogle, and L. Fowler, "Insertable surgical imaging device with pan, tilt, zoom, and lighting," *2008 IEEE International Conference on Robotics and Automation*, pp. 2948–2953, 2008.

[3] S. Platt, J. Hawks, and M. Rentschler, "Vision and task assistance using modular wireless in vivo surgical robots," *Biomedical Engineering, IEEE Transactions on*, vol. 56, no. 6, pp. 1700 –1710, 2009.

[4] P. Valdastri, C. Quaglia, E. Buselli, A. Arezzo, N. D. Lorenzo, M. Morino, A. Menciassi, and P. Dario, "A magnetic internal mechanism for precise orientation of the camera in wireless endoluminal applications.," *Endoscopy*, vol. 42, no. 6, pp. 481–6, 2010.

[5] M. Simi, M. Silvestri, C. Cavallotti, M. Vatteroni, P. Valdastri, A. Menciassi, and P. Dario, "Magnetically activated stereoscopic vision system for laparoendoscopic single-site surgery," *Mechatronics, IEEE/ASME Transactions on*, vol. 18, no. 3, pp. 1140–1151, 2013.

[6] M. Simi, G. Sardi, P. Valdastri, A. Menciassi, and P. Dario, "Magnetic Levitation camera robot for endoscopic surgery," *2011 IEEE International Conference on Robotics and Automation*, pp. 5279–5284, 2007.

[7] M. Sendoh, K. Ishiyama, and K.-I. Arai, "Fabrication of magnetic actuator for use in a capsule endoscope," *Magnetics, IEEE Transactions on*, vol. 39, pp. 3232–3234, Sept 2003.

[8] G. Ciuti, P. Valdastr, A. Menciassi, and P. Dario, "Robotic magnetic steering and locomotion of capsule endoscope for diagnostic and surgical endoluminal procedures," *Robotica*, vol. 28, no. 2, pp. 199–207, 2010.

[9] L. Rossini, O. Chetelat, E. Onillon, and Y. Perriard, "Force and torque analytical models of a reaction sphere actuator based on spherical harmonic rotation and decomposition," *Mechatronics, IEEE/ASME Transactions on*, vol. 18, no. 3, pp. 1006–1018, 2013.

[10] W. Wang, J. Wang, G. Jewell, and D. Howe, "Design and control of a novel spherical permanent magnet actuator with three degrees of freedom," *Mechatronics, IEEE/ASME Transactions on*, vol. 8, no. 4, pp. 457–468, 2003.

[11] Y. Liang, C. I-Ming, Y. Guilin, and L. Kok-Meng, "Analytical and experimental investigation on the magnetic field and torque of a permanent magnet spherical actuator," *Mechatronics, IEEE/ASME Transactions on*, vol. 11, no. 4, pp. 409–419, 2006.

[12] C. Song, A. Alijani, T. Frank, G. Hanna, and A. Cuschieri, "Mechanical properties of the human abdominal wall measured in vivo during insufflation for laparoscopic surgery," *Surgical Endoscopy And Other Interventional Techniques*, vol. 20, no. 6, pp. 987–990, 2006.

[13] J. D. Jackson, *Classical electrodynamics*. New York, NY: Wiley, 1999.

[14] M. Kummer, J. Abbott, B. Kratochvil, R. Borer, A. Sengul, and B. Nelson, "Octomag: An electromagnetic system for 5-dof wireless micromanipulation," *Robotics, IEEE Transactions on*, vol. 26, no. 6, pp. 1006–1017, 2010.

[15] X. Wang and M. Meng, "Dipole modeling of magnetic marker for capsule endoscope localization," in *The 6th World Congress on Intelligent Control and Automation*, vol. 2, pp. 5382–5386, 2006.